# Organogel Assisted Porous Organic Polymer Embedding Cu NPs for Selectivity Control Semi Hydrogenation of Alkynes

Ratul Paul,[a,b,h] Subhash Chandra Shit,[a,b,h] Arunima Singh,[c,h] Roong Jien Wong,[d] Duy Quang Dao,[e,f] Boby Joseph,[g] Wen Liu,*[,d] Saswata Bhattacharya*[,c] and John Mondal*[,a,b]

[a]Catalysis & Fine Chemicals Division, CSIR-Indian Institute of Chemical Technology, Uppal Road, Hyderabad 500 007, India. E-mail: johncuchem@gmail.com; johnmondal@iict.res.in (J.M.)

[b]Academy of Scientific and Innovative Research (AcSIR), Ghaziabad-201002, India.

[c]Department of Physics, Indian Institute of Technology Delhi Hauz Khas, New Delhi 110 016, India. E-mail: saswata@physics.iitd.ac.in (S.B.)

[d]School of Chemical and Biomedical Engineering, Nanyang Technological University, 62 Nanyang Avenue, Singapore 637459. E-mail: wenliu@ntu.edu.sg (W.L.)

[e]Institute of research and development, Duy Tan University, Da Nang, 550000, Viet Nam.

[f] Faculty of Environmental and Chemical Engineering, Duy Tan University, 550000, Da Nang, Viet Nam.

[g]Elettra-Sincrotrone Trieste, S.S. 14, Km 163.5 in Area Science Park, Basovizza 34149, Italy

[h]All the three authors have equally contributed in the manuscript.

**†Electronic supplementary information (ESI) available:** Characterization techniques, computational details, experimental section, $N_2$-sorption, pore size distribution, thermo gravimetric analysis (TGA), optimized structures, $^{13}C$ Cross Polarization (CP) solid state MAS NMR, FE-SEM images, energy dispersive X-ray (EDX) spectroscopy, wide angle powder X-ray diffraction patterns of fresh catalysts, X-ray photoelectron spectroscopy (XPS), temperature and pressure profiles, solvent effect, recyclability test, wide angle powder X-ray diffraction patterns of reused catalysts, XPS and TEM of reused catalysts, table for adsorption energies.

**Abstract**

Heteroatom-rich porous-organic-polymers (POPs) comprising of highly cross-linked robust skeletons with high physical and thermal stability, high surface area, and tunable pore size distribution have garnered significant research interests for their versatile functionalities in a wide range of applications. Here, we report a newly developed organogel-assisted porous-organic-polymer (POP) supported Cu catalysts (**Cu@TpRb-POP**). The organogel was synthesized *via* temperature induced gelation strategy, employing Schiff-base coupling between 2,4,6-triformylphloroglucinol aldehyde (**Tp**) and pararosaniline base (**Rb**). The gel is subsequently transformed to hierarchical porous organic structures without the use of any additive, thereby

offering advantageous features including extremely low density, high surface area, a highly cross-linked framework, and a heteroatom-enriched backbone of the polymer. During the semi-hydrogenation of terminal and internal alkynes, the Cu@TpRb-POP-**B** catalyst with Cu embedded in the TpRb-POP structure consistently demonstrated improved selectivity towards alkenes compared to Cu@TpRb-POP-**A**, which contains Cu NPs exposed at the exterior surfaces of the POP support. Additionally, Cu@TpRb-POP-**B** showed higher stability and reusability than Cu@TpRb-POP-**A**. The superior performance of the Cu@TpRb-POP-**B** catalyst is attributed to the steric hindrance effect, which controls the product selectivity, as well as the synergistic interaction between the heteroatom-rich POP framework and the embedded Cu NPs. Both the effects are corroborated by experimental characterization of the catalysts and density functional theory (DFT) calculations.

**Keywords:** *Organogel, porous organic polymer, semi hydrogenation, terminal and internal alkynes, DFT calculation*

## Introduction

Heteroatom-rich porous-organic-polymers (POPs) that comprise of highly cross-linked robust skeletons, can be used to prepare porous materials with high stability, high surface area, and well-defined pore structures. These POPs can be used as functional support materials for varied applications such as gas storage,[1] photoelectric[2] and heterogeneous catalysts[3]. In present work, we focus on heterogeneous catalysis, whereby by changing the monomer linker, synthetic scheme, reaction media and the molecular connectivity of the POPs, the electronic characteristics of the supported metal can be modulated via metal-support interaction, which in turn tunes the catalytic activities.[5-8] When embedded in the heteroatom-rich microporous POP, the supported metal NPs benefit from the steric hindrance effect, which would control the substrates accessing and the products leaving the metal active sites, rendering enhanced selectivity towards the desired reaction products.

Among the various approaches to synthesize catalysis-relevant POPs, we have chosen an organogel programmed POP synthesis approach, employing low molecular weight organogelators (LMWOGs). This synthetic approach offers numerous advantages over other methods, that includes (i) the synthesis of rigid organogel with very low sol-gel transition temperature, (ii) organogel with very long lifetime because of their high physicochemical and thermal stability. Moreover, various organogels can be developed through this cost effective and simple synthesis procedure with high organogelating LMWOGs. Modification of this technique, by formulating the appropriate combinations of LMWOGs and polymers in a specific solvent opens a new window of opportunity in this field.[9]

Considering the above advantages, we have synthesized nitrogen and oxygen-rich organogel programmed POP (**TpRb-POP**) through a temperature-induced gelation strategy. The subsequent incorporation of Cu nanoparticles (NPs) on the as synthesized **TpRb-POP** using two different approaches, has led to the formation of two catalysts denoted as Cu@TpRb-POP-**A** and Cu@TpRb-POP-**B**. The as-synthesized catalysts were investigated for the semi hydrogenation of alkynes to alkenes. Industrially, this reaction is commonly catalyzed by the Lindlar catalyst, which has many apparent drawbacks associated with its synthesis. This includes the use of porous Pd catalyst in the presence of large amount of quinoline base as additive and the use of toxic lead acetate to suppress the absorption of dihydrogen. In addition, the higher cost and low abundance of noble metals catalyst also hinders the cost competitiveness of the catalytic process.[10] In recent years, significant research efforts have been devoted to develop new catalysts to overcome the drawbacks of Lindlar catalysts.[11,12] Therefore, the development of non-toxic, environmentally friendly, additive-free, noble metal-free catalysts is highly desirable for the semi hydrogenation of alkynes to alkenes.[13] Recently, Cu-based catalysts have received great attention because of their ability to render high selectivity towards alkenes. On the other hand, Cu-based catalysts suffer from several drawbacks, including the harsh reaction conditions (temperature > 473 K) and low catalytic activity.[14] Various catalyst design strategies have been proposed to tackle these limitations, such as (i) preparing bimetallic alloy catalysts consisting of noble[15-21] and non-noble metals[22-25] and (ii) tuning the structure and composition of the support to optimize the electronic and geometric properties of the catalysts *via* metal-support interaction.[13] Moreover, the alkene and alkyne adsorption on the catalytic active sites always play pivotal role in determining the product selectivity. Considering this crucial fact, development of new non-noble metal-based catalysts with active sites capable of selectively adsorbing alkyne becomes utterly important.

In this regard, we have developed two non-noble metal-based Cu catalysts (Cu@TpRb-POP-**A** and Cu@TpRb-POP-**B**) with different structures and distributions of the active sites. Using the semi hydrogenation of phenylacetylene as a model reaction, we show that the unique structural functionality of the Cu@TpRb-POP-**B** catalyst, could effectively boost the reaction selectivity towards alkenes compared to other Cu-based catalysts. Further, the origin of the promoted alkene selectivity is investigated both experimentally and computationally, by in situ diffusive reflectance infrared Fourier-transform spectroscopy (*in situ* DRIFTS) analysis and density functional theory (DFT) calculations, respectively.

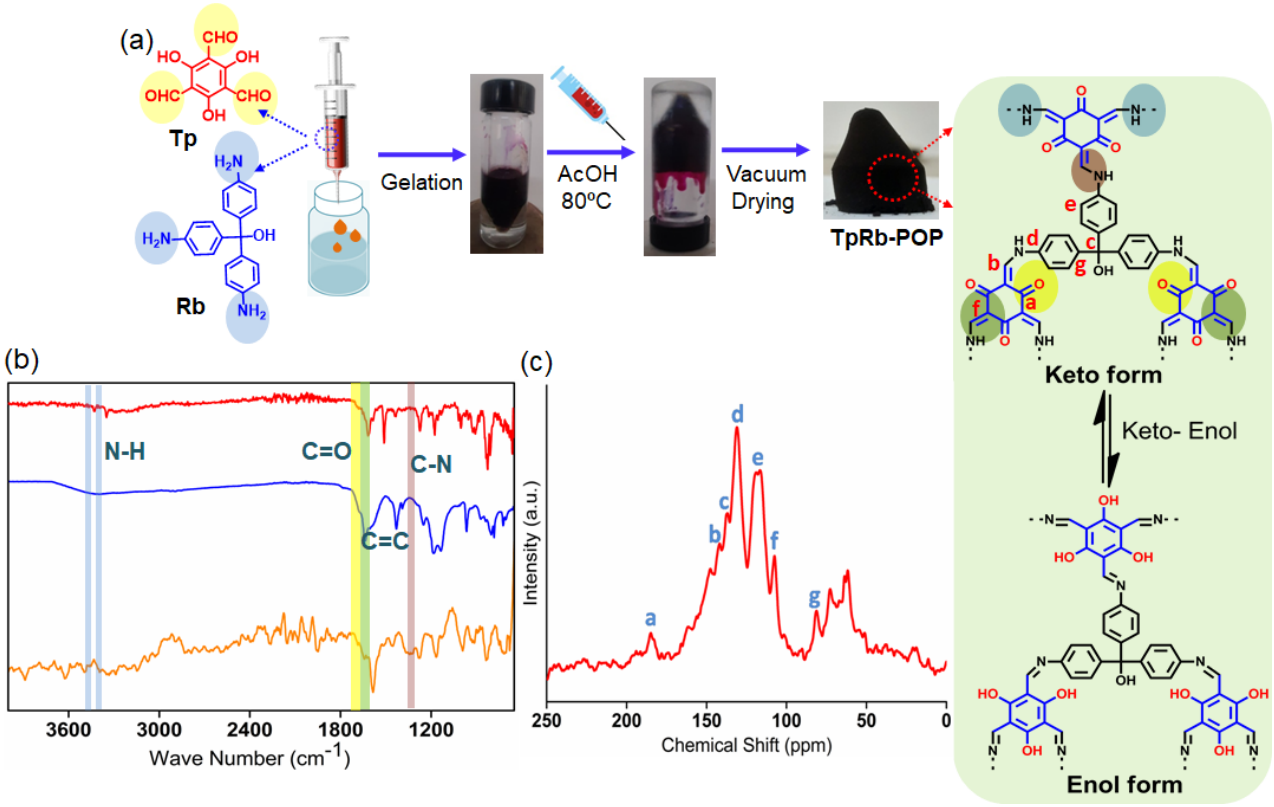


**Figure 1**: (a) Schematic illustration for the synthesis of Organogel induced Porous-Organic-Polymer (**TpRb-POP**); (b) FT-IR spectra of TpRb-POP and its monomers; (c) $^{13}C$ CP solid state MAS NMR spectrum of the as-synthesized **TpRb-POP**.

## RESULT AND DISCUSSION

### Structural Characterization

Figure 1a schematically depicts the synthesis of the organogel-based Porous-Organic-Polymer (**TpRb-POP**) using a temperature induced gelation strategy, via a Schiff-base reaction between pararosaniline base (**Rb**) and 2,4,6-triformylphloroglucinol (**Tp**) aldehyde.[26] The detailed synthesis procedure is provided in the experimental section of the Supporting Information. To monitor the formation of the β-ketoenamine fragment in the **TpRb-POP**, Fourier-transform infrared (FT-IR) spectra of the monomers and the TpRb polymer were measured, as shown in Figure 1b. The observation of the characteristic stretching frequency bands, viz. C=O ~1640 $cm^{-1}$, C=C ~1581 $cm^{-1}$ and C-N ~1272 $cm^{-1}$, are evidence of the formation of β-ketoenamine, generated by enol-keto tautomerization. Moreover, the disappearance of the bands at ~3422 $cm^{-1}$ and 3350 $cm^{-1}$, which correspond to the N-H stretching of **Rb** precursor, indicates the complete conversion of the monomeric units.[27] $N_2$ adsorption-desorption isotherms of **TpRb-POP** at 77 K (Figure S1, SI) exhibit typical type-II isotherm profile with minimal hysteresis and sharp gas uptake at low pressures ($p/p_0$ = 0.0-0.04), followed by the saturation of $N_2$ over the region with $p/p_0$ = 0.27-0.7, suggesting the microporous nature of the sample.[28] A steep rise of $N_2$ uptake at high relative pressures ($p/p_0$ >0.8), suggest the presence of some mesopores, which are attributed to the void

spaces between the POP particles.[29] The specific (Brunauer-Emmett-Teller) BET surface area was estimated to be 383.4 $m^2g^{-1}$, with the corresponding BJH pore volume of 0.451 $cm^3g^{-1}$. The pore-size distribution, determined by nonlocal density functional theory modeling (NLDFT), confirms a narrow pore size distribution, with predominately micropores (1.31 nm) accompanied by a shoulder peak (2.72 nm) in the mesopores region (Figure S2, SI). The molecular connectivity and chemical environment of the carbon nuclei of **TpRb-POP** are probed by $^{13}C$ CP solid state MAS NMR spectroscopy. The results of the MAS NMR, as shown in Figure 1c, exhibits a strong resonance peak at 81.2 ppm, which is attributed to the aliphatic carbon atoms having hydroxy (-OH) groups. The appearance of the characteristic signal at 142.1 ppm corresponds to the imine carbon atom (-C=N) of the aldehyde core of 2,4,6-triformylphloroglucinol (**Tp**).[30] Interestingly, we have also observed two distinctive peaks at 117.8 and 107.1 ppm, respectively, which is attributed to the unsubstituted $sp^2$ carbon atom of the pararosaniline base (**Rb**) moiety and the exocyclic carbons at (-C=C). In addition, the signature bands at 137.4 and 130.9 ppm unambiguously correspond to the C-substituted and the N-substituted $sp^2$ carbon atoms of the pararosaniline base (**Rb**) moiety, respectively. The small peak at ~185 ppm is due to the presence of the (-C=O) group of the β-ketoenamine core.[31] The thermal stability of the as-synthesized **TpRb-POP** was evaluated by thermogravimetric analysis (TGA), as shown in Figure S3, SI. Upon heating to 500 °C under a $N_2$ atmosphere, the thermogram shows two major weight loss peaks at 200 ºC and 420 ºC. Here, the relative weight loss of ~12% up to 200 ºC is associated with the evaporation of the entrapped solvents and gas molecules inside the polymeric framework. At ~420 ºC, a substantial weight loss of ~25% was registered and attributed to the collapse of the entire polymeric network, accompanied by the release of small molecules such as $CO_2$ and $H_2$.

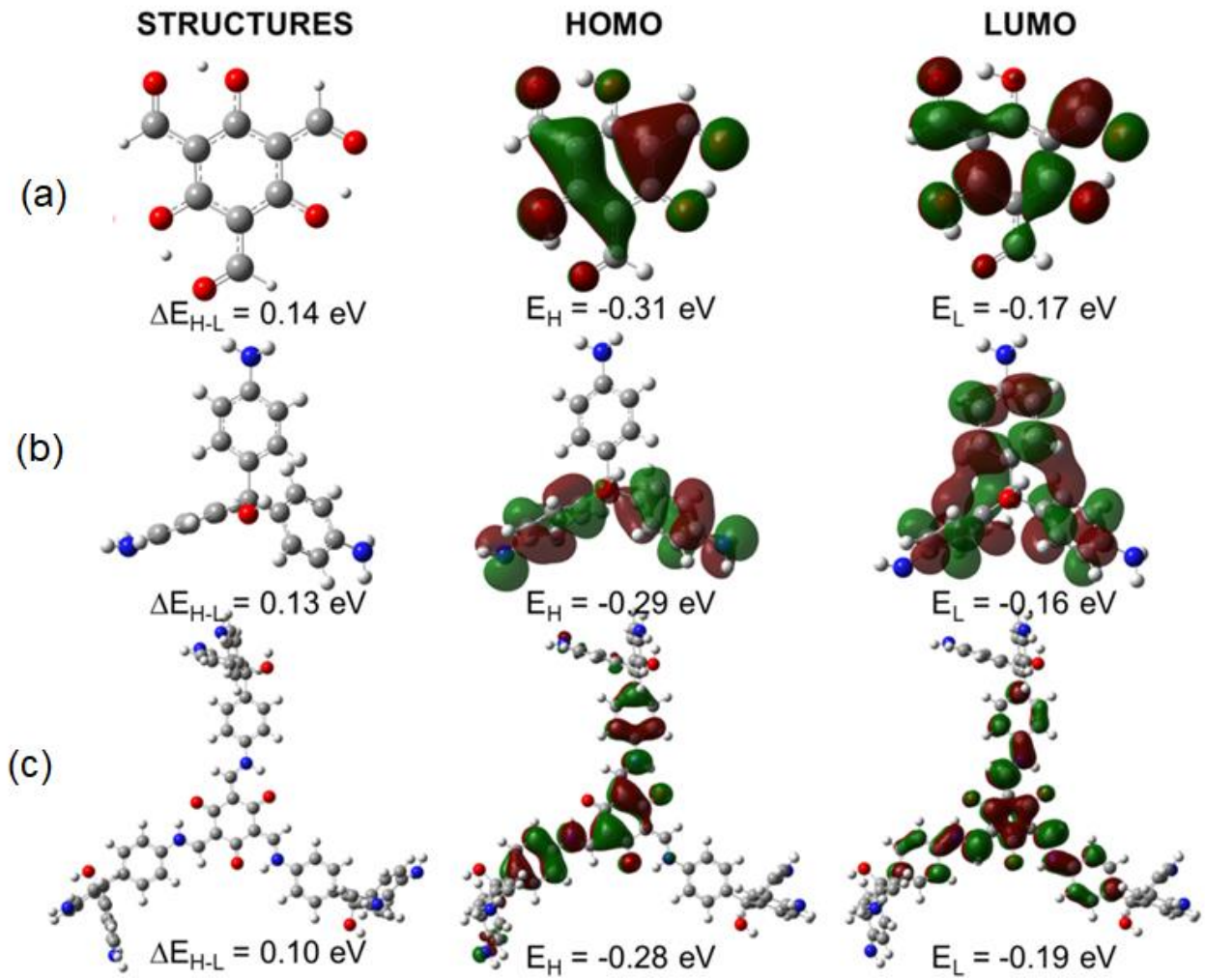


**Figure 2:** Optimized molecular structures, HOMO and LUMO of (**A**) precursor [Tp], (**B**) precursor [Rb] and (**C**) an [A]-3[B] polymer. $E_H$ and $E_L$ represent the energies of the HOMOs and of LUMOs, respectively. $\Delta E_{H-L}$ represents the HOMO-LUMO energy gap. All calculations were performed in the gas phase at the B3LYP/6-31+g (d,p) level of theory.

Figure 2 presents the optimized structures and the distribution of the frontier orbitals, including the highest occupied molecular orbitals (HOMO) and lowest unoccupied molecular orbitals (LUMO) of the monomer precursors and the **TpRb-POP**. These distributions allow characterization of the electron donating-accepting properties of the synthesized polymer. In fact, molecular groups localized the HOMO have a high tendency to donate electrons to external reactants, whereas the ones localized the LUMO have a high tendency to accept electrons. Figure 2 shows that HOMO and LUMO are both delocalized over the benzyl ring of precursor **(a)** (i.e., **Tp**) as well as its hydroxyl (-OH) and aldehyde (-CHO) groups. Moreover, the HOMO is observed over two benzene rings, whereas LUMO is observed over all three benzyl rings (for LUMO) of precursor **(b)** (i.e., **Rb**). The optimized structure of one repeating unit of **TpRb-POP** (Figure 2c) is made from one **(a)** molecule of **Tp** with three **(b)** molecules of **Rb**. It is worth noting that the HOMO of

the polymer is distributed over the molecular chain **(b)-(a)-(b)**, while the LUMO is spread throughout the entire structure of the polymer, especially at the benzyl ring of **(a)**.

The band gap is an important quantum parameter describing the energy discrepancy of valence band and the conduction band.[32] Accordingly, the band gaps of the precursors and the polymer studied are computed. The calculated results, shown in Table S1, suggest that polymerization increased the energy of the HOMO ($E_H$), i.e., from -0.31 and -0.29 eV to -0.28 eV, and decreased the energy of the LUMO ($E_L$) from -0.17 and -0.16 eV to -0.19 eV. Thus, the band gap ($\Delta E_{H-L}$) of the polymer (i.e., 0.10 eV) is remarkably less than those of the precursors (i.e., 0.14 and 0.13 eV for **(a)** and **(b)**, respectively).

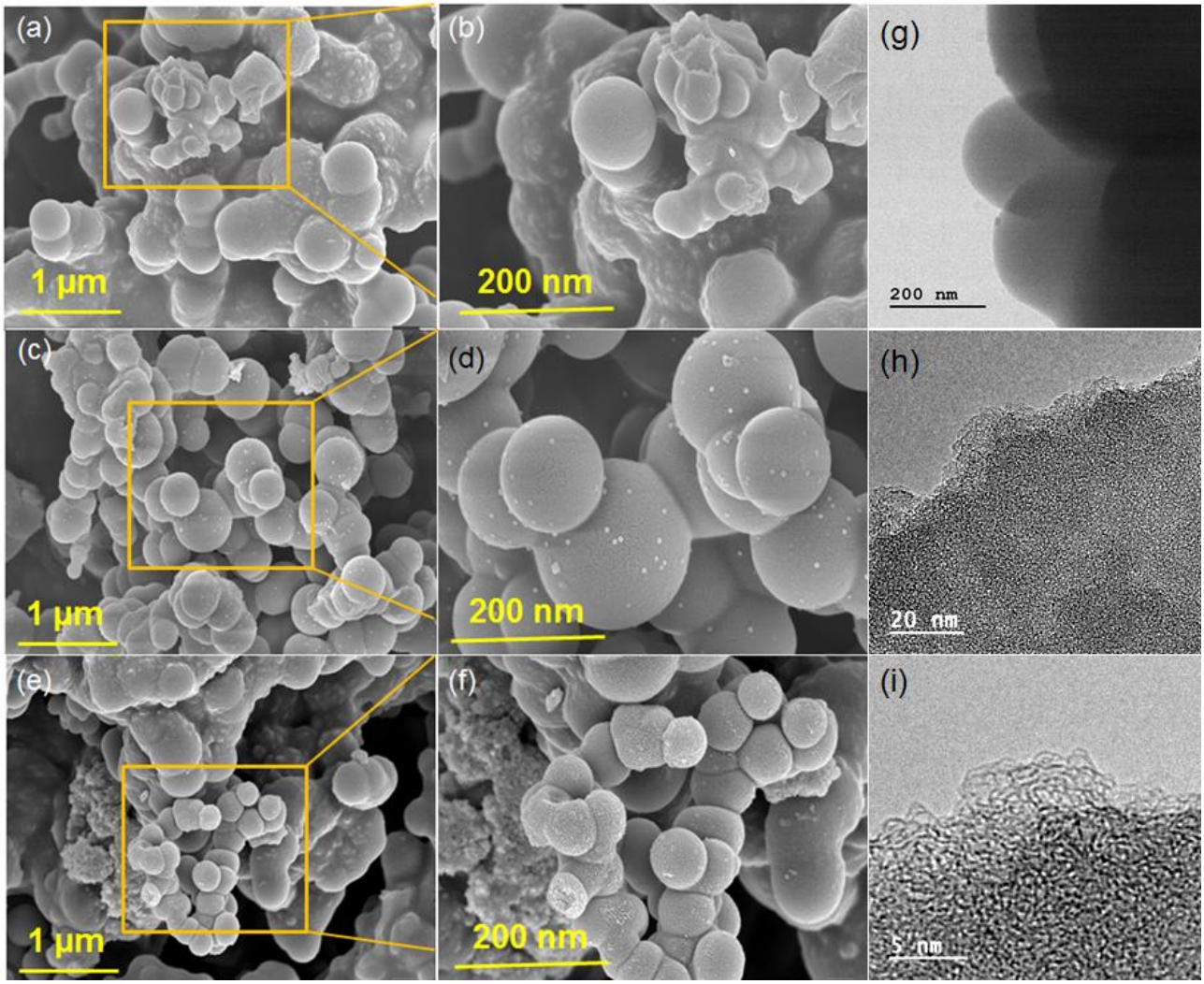


**Figure 3:** FE-SEM images of **TpRb-POP** (a & b), Cu@TpRb-POP-**A** (c & d) and Cu@TpRb-POP-**B** (e & f). HR-TEM images of **TpRb-POP** (g, h & i).

The as-synthesized **TpRb-POP** comprises of -OH and -C=N substituted benzene nodes, with the core units connected through extended π-electron conjugation. The resulting rigid skeletons are exploited as porous nanocages (as shown in Figure 3 h and i) to embed Cu NPs (NPs). The dark brown color product of Cu(II)@TpRb-POP catalysts was isolated by the reaction between **TpRb-POP** and an aqueous solution of $Cu(NO_3)_2.3H_2O$ at room temperature for 12 h. The Cu(II) impreg-

nated **TpRb-POP** precursor was reduced by a liquid phase method or a gas phase method. In the liquid phase method, the precursor was reduced using an ice-cold $NaBH_4$ solution under continued stirring at room temperature for 12 h. In the gas-phase method, the precursor was reduced in a flow of $H_2/N_2$ (10% $H_2$, 100 mL $min^{-1}$) at 250 ºC for 3 h. Both the liquid phase method and the gas phase method yielded black color catalysts, denoted as Cu@TpRb-POP-**A** and Cu@TpRb-POP-**B**, respectively. However, the nucleation and the growth of NPs depends on various factors including support, solvent and the reducing agent used in the particular case.[33,34] Reduction by $NaBH_4$ is one of the most commonly used wet synthesis technique. We have employed electrostatic stabilization method to reduce the Cu ion to zero and thereafter, adsorbed on borohydride ion in order to create electrical double layer to prevent particle aggregation and stabilize them. In addition, these borohydride adsorbed Cu NPs become hydrogen source during the hydrogenation reaction.[35] On the other hand, the $NaBH_4$ is used for reduction is typically dissolved in the hydrophilic $H_2O$ or MeOH, whereas the porous polymeric framework is mostly hydrophobic. Therefore, the precipitation of the Cu precursors, upon reduction of the Cu(II) ions by $NaBH_4$, is restricted to the exterior surface of the POP particles. Hence, the resulting Cu@TpRb-POP-**A** catalyst consists of Cu NPs deposited on the exterior surface of the porous polymer support. In contrast, the solid-phase reduction with the controlled flow of $H_2/N_2$ gas leads to the emergence of core shielded Cu NPs, thereby constructing the unique encapsulated feature by the POP framework, as showed from the TEM images (Figure 4 e and f). This encapsulation restricts the access of reactants to the Cu cluster, mimicking the steric hindrance effect for our **Cu@TpRb-POP-B** catalyst. The aforementioned synthesis scheme is in good agreement with the report by Wang *et. al.*, where the size and dispersion of Pd-NPs inside the POPs were controlled by using different reduction procedures.[36] The supportive evidence by $^{13}C$ CP MAS NMR (Figure S4, SI) revealed that the characteristic resonance signals and stretching vibrations of the POP framework remain unaltered after functionalization with Cu. To examine the morphology of the as-synthesized samples (including **TpRb-POP**, Cu@TpRb-POP-**A** and Cu@TpRb-POP-**B**), FE-SEM and TEM were performed. FE-SEM images of the as-synthesized **TpRb-POP** (Figure 3a & 3b) clearly show that the material is composed of nanospheres having smooth surfaces with diameters ranging from 0.8 to 1µm, forming globular clusters. Lower magnification FE-SEM images of Cu@TpRb-POP-**A** (Figure 3c & S6, SI) and Cu@TpRb-POP-**B** (Figure 3e & S7, SI) showed that these materials have comparatively larger interconnecting spheres (with rough surfaces) with an average diameter of ~1µm. However, the higher magnification FE-SEM image of Cu@TpRb-POP-**A** (Figure 3d) shows the deposition of Cu NPs on the surface of POP, which is absent for Cu@TpRb-POP-**B** (Figure 3f). This finding distinguishes the two catalysts on the basis of surface exposure of Cu NPs thereby indicating its influence on the catalytic activity. Therefore, the two main factors for catalytic activity are the interaction of Cu nanostructure with the reactant and

thermodynamic feasibility. To verify the elemental composition of the nano-structured catalysts, we carried out energy dispersive spectroscopy (EDS) mapping of the as-synthesized samples (Figure S8, SI). The results confirm the presence of Cu (pink) and O (green) in both Cu@TpRb-POP-**A** and Cu@TpRb-POP-**B**. Low magnification TEM images of the as-synthesized **TpRb-POP** (Figure S5, SI) also reveal similar spherical morphology with an average diameter of ~0.9 µm, consistent with the FE-SEM images. Additionally, the HR-TEM images (Figure 3h & 3i) of the **TpRb-POP** materials clearly demonstrate the presence of micropores on the G-POP framework; this is consistent with the $N_2$- adsorption/desorption isotherms.[37-39]

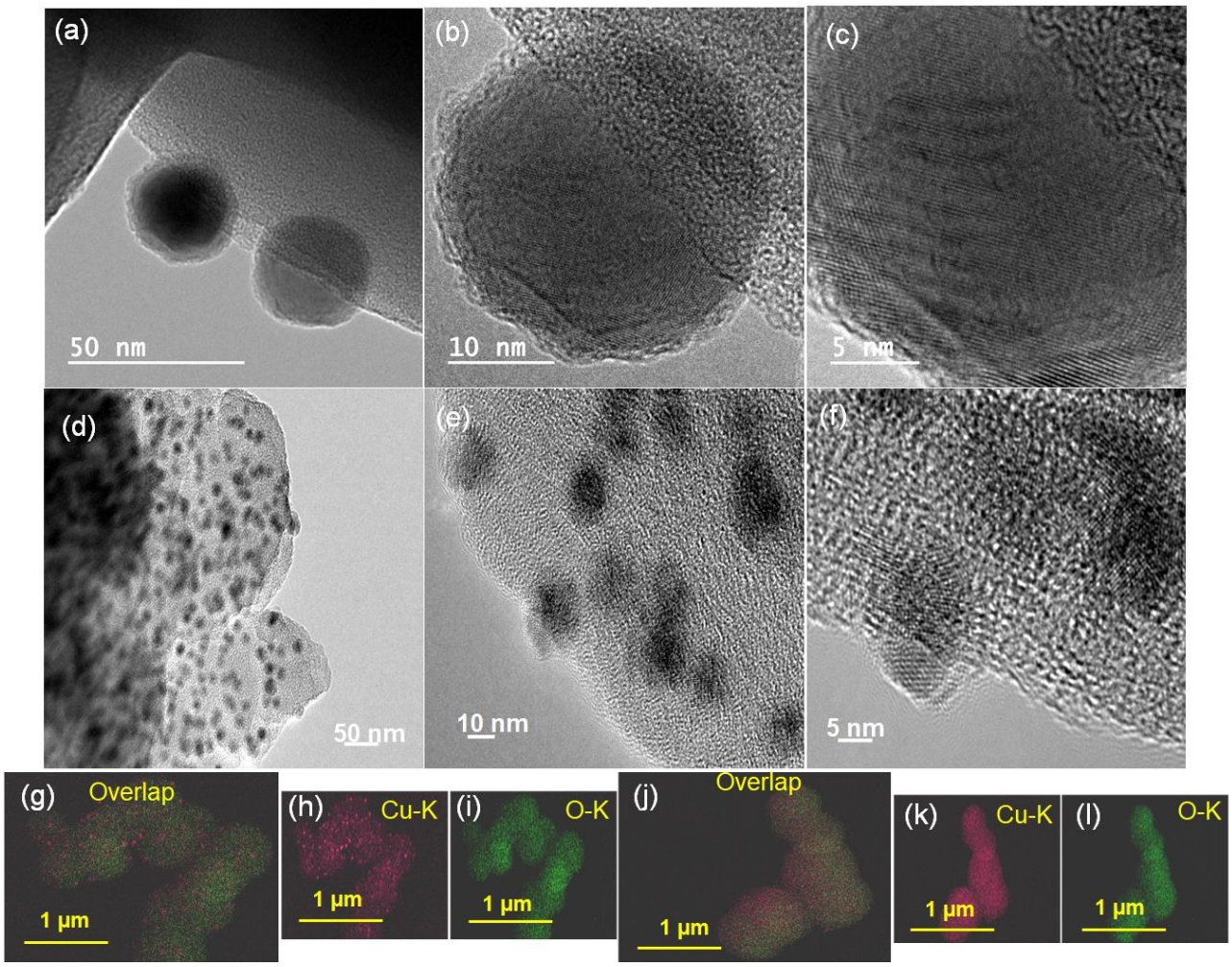


**Figure 4:** TEM images of Cu@TpRb-POP-**A** (a, b & c) & Cu@TpRb-POP-**B** (d, e & f). EDS elemental mappings of (g - i) Cu@TpRb-POP-**A** and (j - l) Cu@TpRb-POP-**B**.

The TEM images of Cu@TpRb-POP-**A** (Figure 4a, b & c) clearly show well dispersed Cu-NPs with uniform particle size distribution between 10-40 nm, exposed on the external surface of the POP support. Unlike Cu@TpRb-POP-**B**, showed a nonuniform dispersion of Cu-NPs with smaller sizes of 8-22 nm (Figure 4d-f). The Histogram profiles for Cu@TpRb-POP-**A** and Cu@TpRb-POP-**B** are provided in Figure S10, SI. In effect, the Cu NPs in Cu@TpRb-POP-**B** are strappingly shielded beneath the carbon layers of the organic polymer shells. Similar findings have

been reported by Maji *et al*., who achieved uniform cobalt dispersion in the azo-naphthalene diimide based POP.[40] Here, the TEM analyses only 2D image of the specimen, the 3D nanostructure of exposed Cu NPs could not be illustrated with this method.[41] Indeed, the EDS elemental mapping of Cu@TpRb-POP-**A** (Figure 4g) & Cu@TpRb-POP-**B** (Figure 4j) revealed that the Cu (red) & O (green) elements are uniformly distributed over the porous organic polymer matrix. Inductively coupled plasma-optical emission spectroscopy (ICP-OES) analysis indicate that the Cu loading in the Cu@TpRb-POP-**A** and Cu@TpRb-POP-**B** catalysts are comparable, at 8.35 and 8.30 wt%, respectively. The wide angle powder X-ray diffraction (PXRD) patterns of the copper loaded **TpRb-POP** (Figure S9, SI) exhibited broad diffractions peaks at $2\theta = 22.3^{o}$, which could be attributed to the π-stacking of the aromatic building blocks in small domains, confirming the preservation of the amorphous framework of the as-synthesized **TpRb-POP**.[42] The PXRD of the two catalysts also exhibit diffraction peaks at 43.3° and 50.5°, which correspond to Cu(111) and Cu(200) reflections, respectively. The broadening of the Cu peaks is similar for both samples, suggesting the size of the Cu NPs in Cu@TpRb-POP-**B** may be comparable to that in Cu@TpRb-POP-**A**. Furthermore, the crystallite sizes (d) for both the catalysts have been calculated from PXRD data using Scherrer equation, which showed good resemblance with the TEM images analysis. The Cu@TpRb-POP-**A** & Cu@TpRb-POP-**B** exhibited 21.0 & 20.9 nm crystallite sizes, respectively.

To find out the surface composition and the metal-support interaction of the Cu@POP catalysts, the samples are examined by X-ray photoelectron spectroscopy (XPS). For the N-1s XPS (Figure S11, SI), the binding energy peak at ~399.4 eV is associated with the N-atom attached to the benzene ring of the pararosaniline base monomer *via* the C-C=N- unit in the enol form. The N-1s XPS peak at ~400.8 eV corresponds to the -NH group in the keto form of the polymer.[43-45] In the O-1s XPS spectra (Figure S12, SI), we observe two characteristic peaks located at ~531.3 eV and ~533.2 eV, which could be assigned to the C=O group in the keto form of polymeric unit and the O atom of C-OH group present in the pararosaniline unit, respectively.[46,47] The deconvoluted Cu-$2p_{3/2}$ XPS spectra (Figure 5a & 5b) for both the materials demonstrates distinctive binding energy peaks at around ~932.6-932.9 eV correspond to the Cu-Cu bond in $Cu^0$ oxidation state.[48] Here it is noteworthy that a significant peak shifting of ~0.3 eV, mainly due to the use of different synthetic approach to generate $Cu^0$ species, is in good agreement with the previous report by Sarkar *et al*.[49] The characteristic binding energy peaks correspond to Cu-$2p_{3/2}$ species are found to be at ~934.5 and 934.4 eV respectively for Cu@TpRb-POP-**A** & Cu@TpRb-POP-**B**. In both the samples, there is a shake-up satellite peak at ~944 eV, which is attributed to the presence of Cu-O bond in CuO species. This CuO species may be confined only to a very thin surface layer, thus allowing its visibility in a highly surface sensitive XPS probe.[50] Moreover, Cu-$2p_{1/2}$ core-level XPS peaks at ~954.3

and 954.2 eV are exhibited for $Cu^{2+}$, whereas the other peaks at ~952.6 and 952.4 eV are assigned to $Cu^{1+}$ species, which are in good agreement with the assignments report by Bui *et al.*[51] Cu 2p XPS show a distinct difference in Cu oxidation states between Cu@TpRb-POP-**A** and Cu@TpRb-POP-**B**. When synthesized by $NaBH_4$ reduction, Cu@TpRb-POP-**A** showed a strong presence of $Cu^{2+}$ state (~934.5 eV) with a smaller fraction of $Cu^0/Cu^+$ state (~932.5 eV). The $Cu^{2+}$ was likely to be in the form of $Cu(OH)_2$ as suggested by the shape of the satellite peak from 938-944 eV. The presence of $Cu^{2+}$ or $Cu(OH)_2$ was attributed to atmospheric oxidation during sample storage and transfer for XPS analysis, as well as the lack of heat treatment to remove moisture during synthesis. The satellite peak also lacked the $Cu^+$ feature at ~945 eV, suggesting the $Cu^0/Cu^+$ component in Cu@TpRb-POP-**A** was highly metallic. In contrast, Cu@TpRb-POP-**B** exhibited a much stronger $Cu^0/Cu^+$ peak, with a ~0.3 eV negative peak shift. The negative peak shift suggested the presence of $Cu^+$ state, which was confirmed by the presence of $Cu^+$ satellite feature. The negative peak shift could also be due to a stronger metal-support interaction, allowing charge transfer from the POP support to the Cu nanoparticles, hence increasing the electron density at the interfacial Cu sites or partially reducing the $Cu^{2+}$ states. The stronger metal-support interaction was achieved by the high temperature reduction step during synthesis.

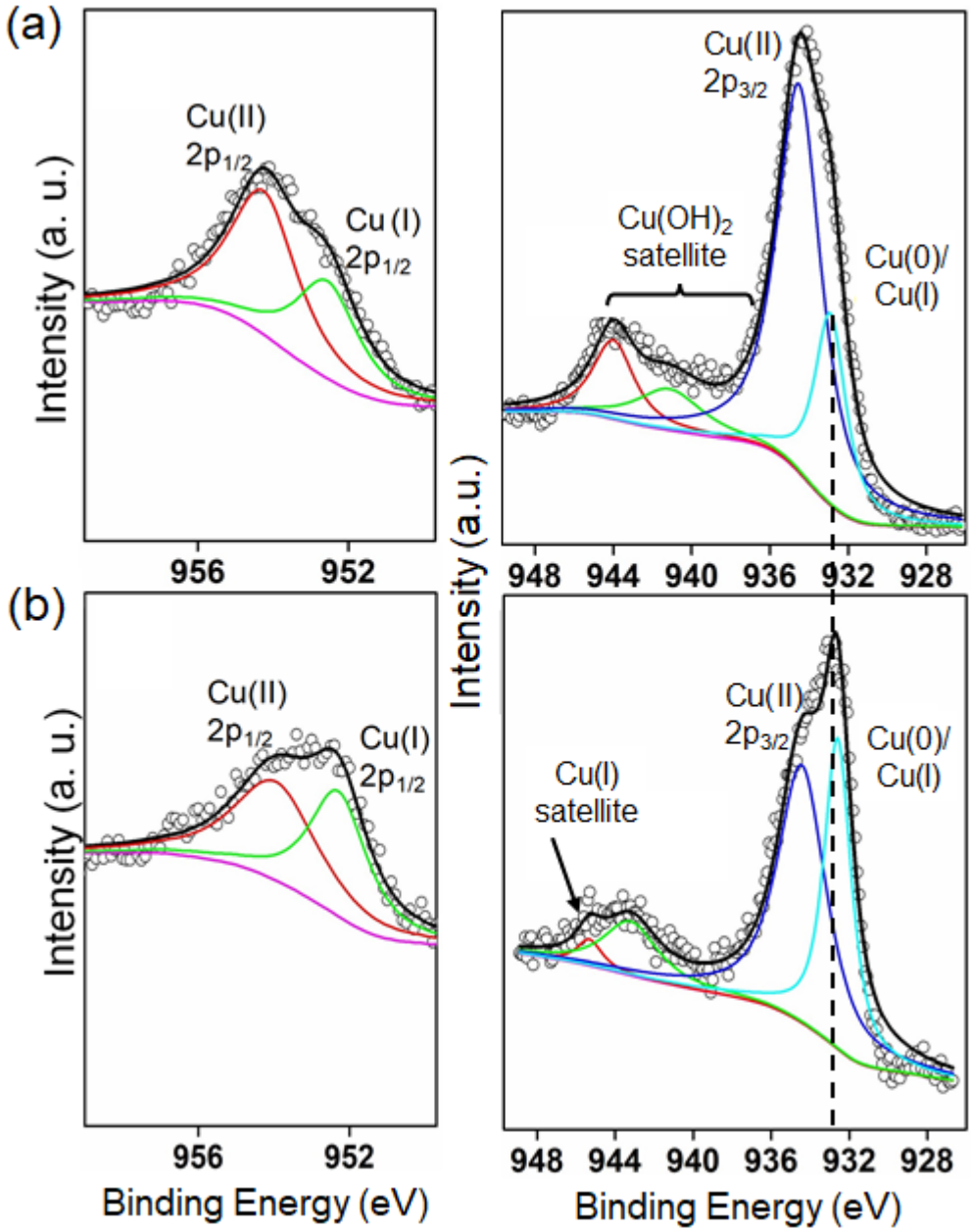


**Figure 5:** Core-level XP spectra of Cu-2p (a, b) for Cu@TpRb-POP-**A** & Cu@TpRb-POP-**B**, respectively.

**Catalytic Activity**

The newly developed catalysts Cu@TpRb-POP-**A** and Cu@TpRb-POP-**B** were evaluated for the semi hydrogenation of phenylacetylene to styrene, with the over-hydrogenated byproduct of ethylbenzene, as schematically illustrated in Figure 6a. Figure 6b and 6c presents the time courses of the hydrogenation reaction on Cu@TpRb-POP-**A** and Cu@TpRb-POP-**B**, respectively. For Cu@TpRb-POP-**A**, 8 h of hydrogenation has achieved 68% phenylacetylene conversion, along with 42% styrene yield and 26% ethylbenzene yield. With the Cu@TpRb-POP-**B** catalyst, we attained 60% conversion, along with 41% and 19% yield of styrene and ethylbenzene, respectively. After 10 h, Cu@TpRb-POP-**A** exhibited 100% conversion along with 65% styrene yield (65% selectivity),

whereas Cu@TpRb-POP-**B** showed 93% conversion with styrene 80% yield (86% selectivity). The apparently reduced phenylacetylene conversion over Cu@TpRb-POP-**B** cf. Cu@TpRb-POP-**A** may be explained by the increased mass transfer resistance for the phenylacetylene to access the Cu NPs embedded within the microporous POP matrix. After 12 h, the styrene yield for both catalysts decreased due to the over-hydrogenation of styrene to ethylbenzene. This decrease is more significant for Cu@TpRb-POP-**A** (65 to 54%) than for Cu@TpRb-POP-**B** (from 80 to 76%). Therefore, the maximum yield of styrene is obtained on Cu@TpRb-POP-**B** after 10 h, affording an estimated turnover frequency (TOF) of about $6 \times 10^{-4}$ $s^{-1}$. In comparison, Cu@TpRb-POP-**A** catalyst showed an inferior styrene TOF of $4.3 \times 10^{-4}$ $s^{-1}$ under identical conditions.

Next, we compare our novel Cu@TpRb-POP-**B** catalyst with other Cu-based catalysts, including $Cu(NO_3)_2.3H_2O$, Cu-NPs, Cu-DVAC-1, Cu-SBA-15. The detailed comparison is shown in Table S3, Supporting Information. $Cu(NO_3)_2.3H_2O$ showed the lowest conversion of 12.3%, with 9.6 and 2.7% yield of styrene and ethyl benzene, respectively. Similarly, Cu-NPs (colloidal system) exhibited a low conversion of phenylacetylene (21.6%) with 15.9% styrene yield. Furthermore, two previously reported Cu-NPs based catalysts, Cu-DVAC-1[52] and Cu-SBA-15,[53] exhibited phenylacetylene conversion of 75.8% and 65.4%, with styrene yield of 63% and 58%, respectively. The synthesis procedures of Cu-DVAC-1 and Cu-SBA-15 are given in the Supporting Information along with their TEM images shown in Figure S15 & S16, SI, respectively. Amongst all the catalysts evaluated, the novel Cu@TpRb-POP-**B** catalyst shows the highest conversion, styrene selectivity and styrene yield. Here, the fact that both the Cu@TpRb-POP-**A** and the Cu@TpRb-POP-**B** catalysts show higher phenylacetylene conversion than the fully exposed Cu catalysts (e.g., Cu-NPs) and Cu NPs trapped in other micro- and mesopores materials (e.g., Cu-DAVC-1 and Cu-SBA-15) manifests the presence of beneficial metal-support interaction in the Cu@TpRb-POP catalysts that gives rise to high intrinsic hydrogenation activities. Additionally, to show the superiority nature of the catalyst we have also compared the semihydrogenation activity with other previously reported metal catalysts (Table S6). For examples, Mitsudome *et al.* and Wu *et al.* utilized noble and expensive metal-based catalysts Pd@Ag and PdCuS NPs, respectively, for the semihydrogenation reaction whereas we have used non-noble metal based Cu catalysts.[54,55] On the other hand, Copéret and co-workers although achieved very high alkene selectivity (>94 %) along with full conversion of alkyne employing silica supported Cu nanoparticle as active component for the reaction, but they utilized phosphine based ligand ($PCy_3$) and N-heterocyclic carbene (NHC) ligand as promoter.[56,57] In our case we have not used any kind of ligand promoter. Huang and co-workers also delivered an excellent work by developing non-noble metal-based Cu crystals with face-centered cubic crystal structures for semi hydrogenation, but the disadvantages repose on the recyclability of catalyst.[58]

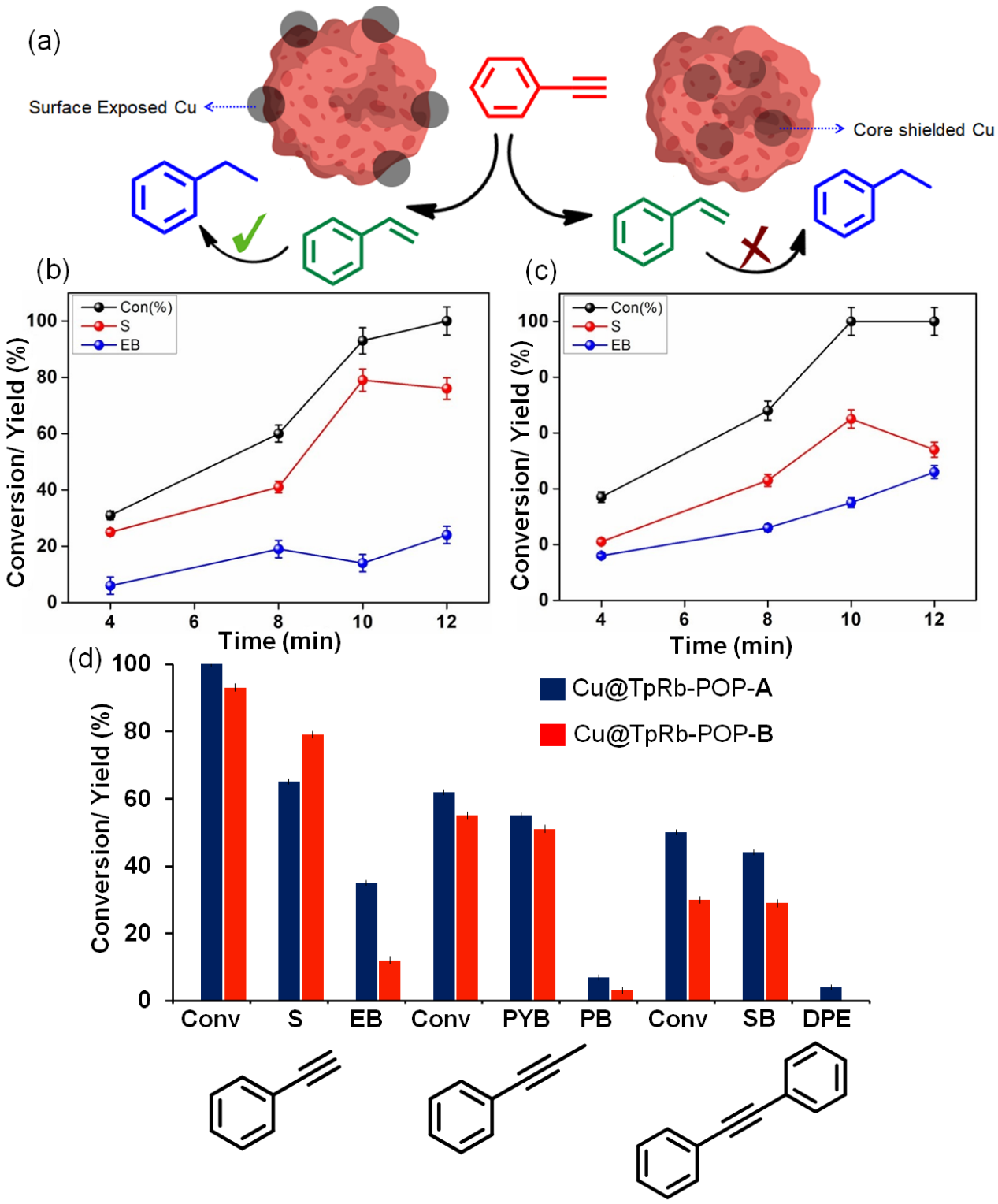


**Figure 6:** (a) Reaction scheme for semi hydrogenation of phenylacetylene. Evolution of reactant and product distributions over time for (b) Cu@TpRb-POP-**A** and (c) Cu@TpRb-POP-**B**, respectively; (d) comparison study with terminal & internal alkynes over two catalysts. (S: Styrene; EB: Ethyl Benzene; PYB: Prop-1-en-1-ylbenzene; PB: Propane Benzene; SB: Stilbene; DPE: Diphenyl Ethane). **Reaction conditions:** Reactant (1 mmol), catalysts (30 mg), isopropanol (30 mL), 2 MPa $H_2$ pressure, 150 °C, Time (10 h).

To further elaborate the superiority of Cu@TpRb-POP-**B**, we evaluated both catalysts for the semi hydrogenation of other terminal and internal alkyne substrates, including phenylacetylene,

1-phenyl-1-propyne and diphenylacetylene; the results are shown in Figure 6d. In all cases, Cu@TpRb-POP-**B** achieved higher alkene yield and lower alkyne conversion than Cu@TpRb-POP-**A**. The observed trends in alkyne conversion and alkene selectivity verify the generality of the selectivity boost effect by the Cu@TpRb-POP-**B** catalyst design, making it a promising low-cost semi-dehydrogenation catalyst. The plausible mechanistic pathway for semi hydrogenation was previously described by Wang and co-workers. They have achieved higher alkene product selectivity by modifying,[12] poisoning[59] and doping[60] the metal active sites (Pd) which reduces the 'C=C' adsorption and simultaneously enhances the alkene selectivity. So, it is quite obvious that the extent of alkene adsorption on the catalytic active sites plays a crucial role and we can always alter the product selectivity for semi hydrogenation by modifying the catalytic active sites. In this regard, to experimentally verify that the Cu@TpRb-POP-**B** catalyst is mechanistically more selective towards styrene than Cu@TpRb-POP-**A**, in situ Diffuse reflectance infrared Fourier-transform spectroscopy (DRIFTS) experiments were performed to examine the interaction between styrene and the catalysts.

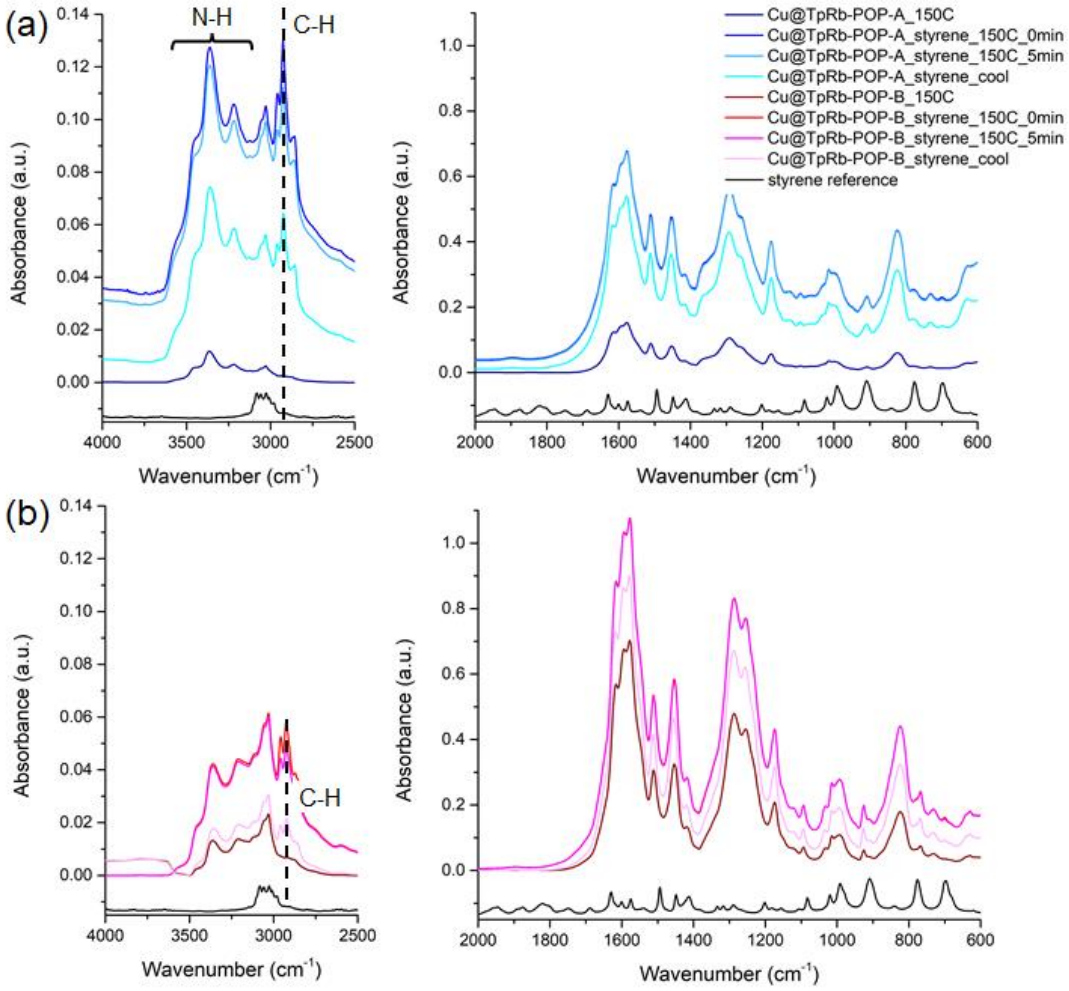


**Figure 7:** In situ DRIFT spectra showing the interaction of styrene with (a) Cu@TpRb-POP-**A** and (b) Cu@TpRb-POP-**B** catalysts in the spectral ranges of (left) 4000-2500 $cm^{-1}$ and (right) 2000-600 $cm^{-1}$.

In general, more interaction between styrene and the catalyst corresponds to stronger adsorption of styrene on the Cu active sites and a greater tendency to produce more over-hydrogenation products of ethylbenzene. The DRIFTS analysis, shown in Figure 7, indicates distinct differences between the catalytic properties of Cu@TpRb-POP-**A** and Cu@TpRb-POP-**B**. Upon introducing styrene at 150 °C, the surface of the Cu@TpRb-POP-**A** sample showed drastic changes, including the emergence of significant absorption peaks in the 2500-4000 $cm^{-1}$ and the 600-2000 $cm^{-1}$ spectral ranges, as shown in Figure 7(a). These peaks are attributed to the chemical interaction between the styrene molecules and the catalyst. The intensities of the absorption signals dropped slightly after 5 min at 150 °C. After cooling down to room temperature, the absorption peaks retained ~50% of their intensities at 150 °C, indicating strong adsorption of styrene. In contrast, the change in the DRIFT spectra of Cu@TpRb-POP-**B** is marginal before and after styrene addition at 150 °C (see Figure 7(b)). Cooling to room temperature caused the intensities of the absorption peak to significantly reduce, producing a spectrum resembles that of the pristine Cu@TpRb-POP-**B**. The absorption peak at ~2925 $cm^{-1}$ is attributed to the C-H bond vibration mode of styrene, while the ~3200-3500 $cm^{-1}$ region is attributed to the N-H group of TpRb-POP. The relative decrease in C-H peak suggest suggests a higher retention rate of styrene on Cu@TpRb-POP-**A** relative to Cu@TpRb-POP-**B**. In summary, the interaction between Cu@TpRb-POP-**B** and styrene is much weaker than that between Cu@TpRb-POP-**A** and styrene. Therefore, the DRIFT results provide mechanistic evidence that the nanostructured Cu@TpRb-POP-**B** with polymer-shielded Cu NPs is an effective catalyst design to hinder the undesirable adsorption of styrene onto the Cu active sites, subsequently boosting the styrene selectivity during the semi-hydrogenation of phenylacetylene.

Figures 8a & 8b show the effect of temperature on the semi hydrogenation. For Cu@TpRb-POP-**A**, increasing the temperature from 150 °C to 160 °C has no impact on phenylacetylene conversion, which remained at 100%. However, the styrene yield substantially decreased from 65 % to 43% with the 10 °C temperature increase, mainly due to the over hydrogenation of styrene to ethyl benzene. In contrast, for Cu@TpRb-POP-**B** (Figure 8b), the temperature increases from 150 °C to 160 °C improved the phenylacetylene conversion from 93% to 100%, accompanied by a small drop in styrene yield (86 to 75%). The higher yield exhibited by the Cu@TpRb-POP-**B** catalyst is ascribed to the restricted access of the reactant molecules to the Cu active sites, which are trapped inside the microporous nanocages.

Figures 8c and 8d show the effect of hydrogen pressure on the semi hydrogenation. For both catalysts, higher hydrogen pressure resulted in improved conversion of phenylacetylene and reduced styrene yield due to over-hydrogenation. Nevertheless, The Cu@TpRb-POP-**B** (selectivity reduced from 86 to 71%) is significantly more resistant to over-hydrogenation than Cu@TpRb-

POP-**A** (selectivity reduced from 65 to 48%), i.e., the unique structure of the Cu@TpRb-POP-**B** is inherently more selective to the semi hydrogenation towards styrene.

When tested in different solvents including isopropanol, methanol, ethanol and toluene, Cu@TpRb-POP-**B** showed consistently better performance, (i.e., similar conversion with significantly higher styrene yield) than Cu@TpRb-POP-**A** (Figure S13 & S14, SI). For each type of Cu@TpRb-POP catalyst, its catalytic activity, in terms of phenylacetylene conversion and styrene yield, in different solvents are similar. In general, the reactions taking place in isopropanol and toluene show the highest and the lowest phenylacetylene conversion, respectively. With both catalysts, the hydrogenation reactions taking place in toluene result in the lowest styrene yield, whereas the reactions in isopropanol generally give the highest styrene yield.

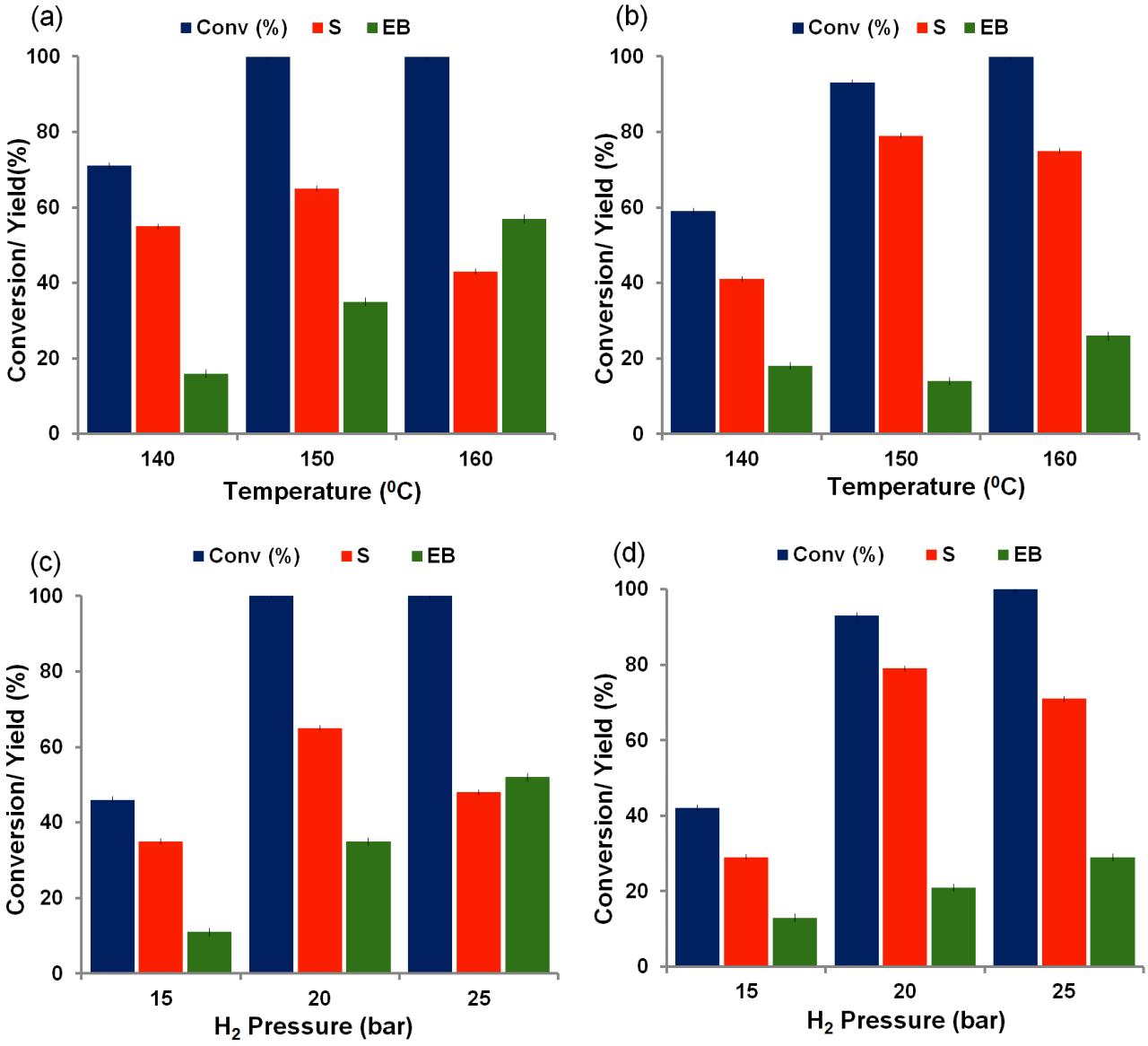


**Figure 8:** (a) & (b) Temperature profile of two catalysts Cu@TpRb-POP-**A** and Cu@TpRb-POP-**B**, respectively; (c) & (d) Effect of pressure on two catalysts Cu@TpRb-POP-**A** and Cu@TpRb-POP-**B**, respectively. **Reaction conditions:** Phenyl Acetylene (PA) (0.11ml, 1 mmol), catalysts (30 mg), isopropanol (30 mL), Time (10 h).

To elucidate the contribution of the organic framework to the apparent catalytic activity and styrene yield, we prepared Cu nanoclusters embedded in carbon supports and tested them for phenylacetylene dehydrogenation under identical conditions (see results in Table S4, SI). Cu NPs were deposited on the carbon support following the similar liquid-phase and solid-gas phase reduction methods, yielding Cu@C-**A** and Cu@C-**B**, respectively, whose TEM images are shown in Figure S16 (a) & (b), SI, respectively. From Figure S17, SI it can be seen that the Cu NPs in Cu@C-**A** are more exposed to the surface, whereas those in Cu@C-**B** are shielded beneath the porous carbon layers. In both catalysts, the sizes of the Cu NPs are similar (~20 ± 1.5 nm). Accordingly, Cu@C-**A** and Cu@C-**B** catalysts achieved phenylacetylene conversions of 76.5 & 72.3% with styrene yields of 71.2 & 67.4%, respectively. Overall, the Cu@C type appears less reactive than the Cu@TpRb-POP type catalyst. However, the Cu@C-**B** catalysts with shielded Cu NPs did not show enhanced alkene yield over the Cu@C-**A** catalyst. Generally speaking, the steric hindrance effect requires microporosity. Therefore, it is inducive that the Cu@C may not be able to offer a structure that could afford sufficient steric hindrance to significantly enhance the yield of phenylacetylene towards styrene. From this experimental evidence, we can unambiguously conclude that the steric hindrance effect offered by the organic functional backbone of POP play a decisive role in controlling the product yield. The Cu@TpRb-POP catalyst could achieve comparable performance to those reported in the literature, but without using any noble metal or additives.

**Computational Investigation**

Density functional theory (DFT) calculations were performed to shed light on the nature of the interaction between the Cu NPs and the TpRb-POP that leads to the improved catalytic performance of Cu@TpRb-POP-**B**. The first step is to elucidate the geometrically optimized structures of the two of Cu-POP-type catalysts. As per experiments, Cu-NPs have been introduced into the POP framework to furnish Cu@TpRb-POP-**A** & Cu@TpRb-POP-**B**. We have optimized the geometrical structures with two different Cu-cluster sizes, to elucidate the effect of Cu particle size as a potential artifact.

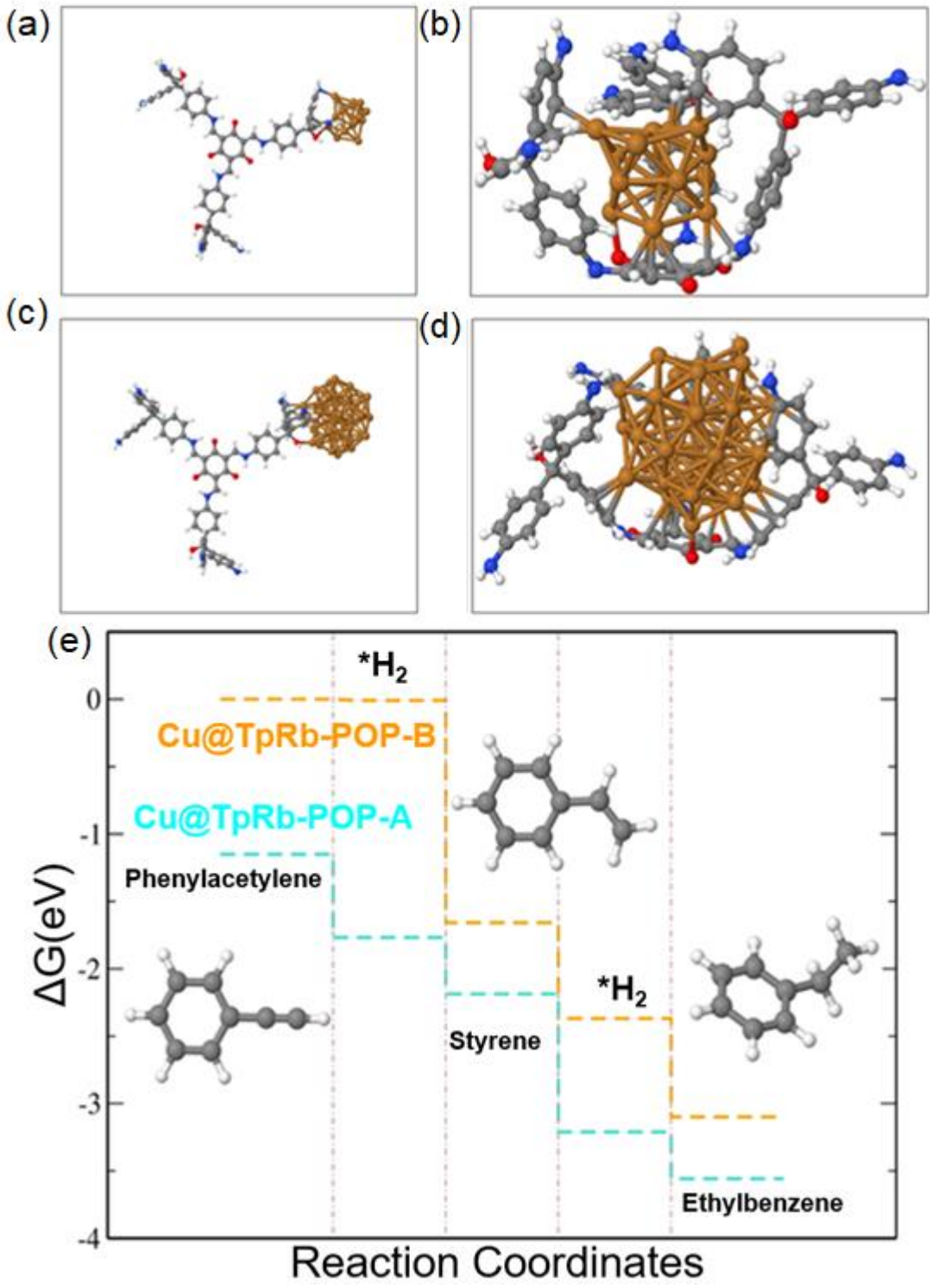


**Figure 9:** (a) and (b): The deposition of a small Cu-cluster ($Cu_{14}$) on Cu@TpRb-POP-**A** and Cu@TpRb-POP-**B**, respectively. (c) and (d): the deposition of a large Cu-cluster ($Cu_{43}$) in Cu@TpRb-POP-**A** and Cu@TpRb-POP-**B**, respectively. (e) Energy profile for the successive hydrogenation of phenylacetylene to styrene and then to ethylbenzene in Cu@TpRb-POP-**A** and Cu@TpRb-POP-**B**. Here the $*H_2$ implies the configuration with dissociated $H_2$ adsorbed on the surface.

Figures 9 a and c put forth the models simulating Cu@TpRb-POP-**A**, in which the Cu-cluster is exposed on the external surface of the POP framework. The Cu-cluster here is modelled from the bulk (3-dimensional fcc structure) Cu. The spatial confinement of the Cu-cluster in Cu@TpRb-POP-**B** is

simulated by the model structures depicted in Figures 9b and d. In the Cu@TpRb-POP-**B** model, the encapsulation by the POP framework will influence the access of the reactants to the Cu cluster, mimicking the steric hindrance effect; such effect is absent in the model for Cu@TpRb-POP-**A**.

Accordingly, we computed the adsorption energy ($E_{ads}$) of phenylacetylene, styrene and ethylbenzene on the geometrically optimized structure of Cu@TpRb-POP-**A** and Cu@TpRb-POP-**B** (Figure 9a & 9b). We observed $E_{ads} < 0$ in all the adsorption configurations (Table S5, SI), suggesting that the proposed structural configurations are energetically favorable. The strong adsorption of phenylacetylene on the Cu@TpRb-POP-**A** catalyst is in agreement with the experimental observation of higher phenylacetylene conversions on Cu@TpRb-POP-**A**.

Irrespective of the size of Cu cluster, the Cu@TpRb-POP-**B** model indulged in more interaction between the Cu and the organic molecule than the Cu@TpRb-POP-**A** model. Therefore, particle size does not appear to affect the nature of the metal-support interaction. The calculated adsorption energies, as shown in Table S5, suggest that the adsorption of styrene on the Cu sites are significantly weakened by the steric hindrance effect shown by the Cu@TpRb-POP-**B** model. In the real Cu@TpRb-POP-**B** catalyst, the Cu cluster is embedded in a bulkier POP skeleton than the model structure shown in Figures 9b and d. Therefore, we expect the steric hindrance effect of the real Cu@TpRb-POP-**B** catalyst to be more profound than in the DFT calculations, affording a significant boost in styrene yield.

We now put forward the energy pathways for the hydrogenation of phenylacetylene on Cu@TpRb-POP-**A** and Cu@TpRb-POP-**B**, as shown in Figure 9e. The free energy change for each reaction step is negative i.e., $\Delta G < 0$, verifying the thermodynamic feasibility. As mentioned previously, the Cu@TpRb-POP-**A** has lower configurational energy as compared to that of Cu@TpRb-POP-**B**. Also, the energy profile (Figure 9e) of the intermediate adsorbates on Cu@TpRb-POP-**A** is lower than those on Cu@TpRb-POP-**B**. This indicates high stability of phenylacetylene, styrene and ethylbenzene molecules on Cu@TpRb-POP-**A**, which results in higher selectivity towards over-hydrogenation to produce ethylbenzene than Cu@TpRb-POP-**B**.

**Catalyst Reusability**

The reusability of the two Cu@TpRb-POP catalysts was evaluated by performing up to seven consecutive batch hydrogenation reactions under similar reaction conditions. The results of the reusability experiments are shown in (Figures S18 and S19, SI). In general, Cu@TpRb-POP-**B** exhibited superior reusability than Cu@TpRb-POP-**A**. The alkyne conversion and alkene yield on Cu@TpRb-POP-**B** marginally decreased (conversion 94% to 83%; yield 79% to 70%), whereas for Cu@TpRb-POP-**A**, the alkene yield decreased from 68% to 47%, along with a drastic drop in conversion (100% to 69%). To probe the origin of the cyclic decay in catalytic activity, the resused catalysts were thoroughly characterized by TEM, XPS and PXRD. From the PXRD patterns of the

recovered catalysts (Figure S20, SI), we do not observe any crystalline phase change to the Cu NPs over the cyclic experiments. However, the Cu peaks in Cu@TpRb-POP-**A** have become much sharper than those of the freshly prepared catalysts, suggesting some extent of sintering. In addition, Cu 2p XPS of the reused Cu@TpRb-POP-**A** (Figure S21, SI) showed significantly different surface chemical states from the fresh catalyst.[61] The binding energy peaks at ~935.4 eV along with the satellite peaks at ~943.7 eV was observed; they might be due to presence of more surface $Cu^{+2}$. Furthermore, the binding energy peaks of $Cu^{0}$ was shifted by ~0.2 eV compared to the fresh catalyst. This shift could be ascribed to the reduced interaction of the Cu NPs with the POP support. The reduced interaction can be correlated to the apparent sintering of the Cu NPs to form larger Cu particles in Cu@TpRb-POP-**A**. For Cu@TpRb-POP-**B**, no notable change in the Cu 2p XPS could be observed after the cyclic test (Figure S19, SI). TEM images of the reused catalysts (Figure S21, SI) clearly show larger Cu particle size on Cu@TpRb-POP-**A** than those on Cu@TpRb-POP-**B** after 7 reaction cycles, supporting the XRD finding that the Cu NPs on Cu@TpRb-POP-**A** have sintered. Another interesting observation is the emergence of surface-exposed Cu NPs on the reused Cu@TpRb-POP-**B** catalyst (Figure S22 d, e & f, SI), this structural alternation is probably responsible for the reduced alkene yield over the consecutive catalytic experiments.[62]

## Conclusion

In this study, we have successfully synthesized organogel assisted heteroatom-rich (N and O) porous organic polymer supported Cu NPs using two different reduction techniques, which results in two different catalyst structures with contrasting catalytic performance. Schiff-base coupling between 2,4,6-triformylphloroglucinol aldehyde and pararosaniline base methodology was employed to develop the organogel. The synthetized catalysts were evaluated for the semi hydrogenation of terminal and internal alkynes. The Cu@TpRb-POP-**B** catalyst, prepared by the gas-phase reduction using a $H_2/N_2$ mixture exhibited greater styrene selectivity (86%) than the Cu@TpRb-POP-**A** catalyst (65%), which was prepared by the liquid-phase reduction using a $NaBH_4$ solution. The selectivity enhancement by Cu@TpRb-POP-**B** is attributed to the fact that the Cu NPs are shielded by the microporous POP support, affording an effective steric hindrance effect that limits the over-hydrogenation of styrene to ethylbenzene. In contrast, the Cu@TpRb-POP-**A** catalyst consists of surface-exposed Cu clusters, which are unselective during the hydrogenation of phenylacetylene. The experimental analyses of the structural-functional relationship are fully corroborated by DFT calculations. In conclusion, the present study has demonstrated the utility of POP materials to serve as effective support for transition metal catalysts and to provide selectivity control by offering steric hindrance effect through its rigid, microporous polymer framework. These findings pave the way towards the rational design of various gel-assisted heteroatom-rich POP

frameworks as environmentally friendly and non-noble metal-based catalysts for a variety of chemical applications.

## Conflicts of interest

There are no conflicts to declare.

## Acknowledgements

R.P. and S.C.S. acknowledge DST-INSPIRE (GAP-0799) and the Council of Scientific and Industrial Research (CSIR), New Delhi, for their respective senior research fellowships. J.M. acknowledges the Department of Science and Technology, India, for the DST-INSPIRE Faculty Research Project Grant (GAP-0522), CSIR-YSA Research Grant (reference no. HRDG/YSA-19/02/21(0045)/2019) & and Focused Basic Research (FBR) Grant under the CLP theme (reference no. 34/1/TD-CLP/NCP-FBR 2020-RPPBDD-TMD-SeMI) for financial support at CSIR-IICT, Hyderabad. We thank the Director, CSIR-IICT (Ms. No. IICT/Pubs./2021/358), for providing all kind of the required facilities to carry out the work.

**References:**


1. J. Jia, Z. Chen, H. Jiang, Y. Belmabkhout, G. Mouchaham, H. Aggarwal, K. Adil, E. Abou-Hamad, J. Czaban-Jo´zwiak, M. R. Tchalala and M. Eddaoudi, *Chem* 2019, **5,** 180-191.

2. H. Bildirir, V. G. Gregoriou, A. Avgeropoulos, U. Scherf and C. L. Chochos, *Mater. Horiz.* 2017,**4**, 546-556.

3. S. C. Shit, I. Shown, R. Paul, K. H. Chen, J. Mondal and L. C. Chen, *Nanoscale* 2020, **12**, 23301-23332.

4. A. Halder, S. Kandambeth, B. P. Biswal, G. Kaur, N. C. Roy, M. Addicoat, J. K. Salunke, S. Banerjee, K. Vanka, T. Heine, S. Verma and R. Banerjee, *Angew. Chem. Int. Ed.* 2016, **55**, 7806-7810.

5. R. Paul, C. Sarkar, Y. Yan, Q. T. Trinh, B. S. Rao, C.-W. Pao, J.-F. Lee, W. Liu and J. Mondal, *ChemCatChem* 2020, **12**, 3687.

6. M. Bhadra, H. S. Sasmal, A. Basu, S. P. Midya, S. Kandambeth, P. Pachfule, E. Balaraman and R. Banerjee, *ACS Appl. Mater. Interfaces* 2017, **9**, 13785-13792.

7. H. Zhang, X. Gu, J. Song, N. Fan and H. Su, *ACS Appl. Mater. Interfaces* 2017, **9**, 32767-32774.

8. J. Liu, J. Cui, F. Vilela, J. He, M. Zeller, A. D. Hunterd and Z. Xu, *Chem. Commun.* 2015, **51**, 12197-12200.

9. M. Suzuki and K. Hanabusa, *Chem. Soc. Rev.* 2010, **39**, 455-463.

10. J. Liu, N. Wang, J. Liu, M. Li, Y. Xu, C. Wang, Y. Wang, H. Zheng and L. Ma, *ACS Appl. Mater. Interfaces* 2020, **12**, 51428-51436.

11. S. P. Desai, J. Ye, J. Zheng, M. S. Ferrandon, T. E. Webber, A. E. Platero-Prats, J. Duan, P. Garcia-Holley, D. Camaioni, K. W. Chapman, M. Delferro, O. K. Farha, J. L. Fulton, L. Gagliardi, J. A. Lercher, R. L. Penn, A. Stein and C. C. Lu, *J. Am. Chem. Soc.* 2018, **140,** 15309-15318.

12. Q. Luo, Z. Wang, Y. Chen, S. Mao, K. Wu, K. Zhang, Q. Li, G. Lv, G. Huang, H. Li and Y. Wang, *ACS Appl. Mater. Interfaces* 2021, **13**, 31775-31784.

13. T. Yoshii, D. Umemoto, Y. Kuwahara, K. Mori and H. Yamashita, *ACS Appl. Mater. Interfaces* 2019, **11**, 37708-37719.

14. Z. Guan, M. Xue, Z. Li, R. Zhang and B. Wang, *Appl. Surf. Sci.* 2020, **503**, 144142.

15. A. J. McCue, C. J. McRitchie, A. M. Shepherd and J. A. Anderson, *J. Catal.* 2014, **319**, 127-135.

16. H. Wang, Q. Luo, W. Liu, Y. Lin, Q. Guan, X. Zheng, H. Pan, J. Zhu, Z. Sun, S. Wei, J. Yang and J. Lu, *Nat. Commun.* 2019, **10**, 4998.

17. J. Yang, M. Yuan, D. Xu, H. Zhao, Y. Zhu, M. Fan, F. Zhang and Z. Dong, *J. Mater. Chem. A* 2018, **6**, 18242-18251.

18. R. L. Oliveira, J. Kerstien, R. Schomäckerb and A. Thomas, *Catal. Sci. Technol*. 2020, **10**, 1385-1394.

19. Q. Li, Y. Wang, G. Skoptsov and J. Hu, *Ind. Eng. Chem. Res.* 2019, **58**, 20620-20629.

20. E. Park, J. Jack, Y. Hu, S. Wan, S. Huang, Y. Jin, P. C. Maness, S. S. Yazdi, Z. Ren and W. Zhang, *Nanoscale* 2020, **12**, 2596-2602.

21. S. L. Lu, Y. Hu, S. Wan, R. McCaffrey, Y. Jin, H. Gu and W. Zhang, *J. Am. Chem. Soc.* 2017, **139**, 17082-17088.

22. Y. Liu, J. Zhao, J. Feng, Y. He, Y. Du and D. Li, *J. Catal.* 2018, **359**, 251-260.

23. X. Yang and Q. Xu, *Trends Chem.* 2020, **2**, 214-226.

24. R. Tao, X. Shen, Y. Hu, K. Kang, Y. Zheng, S. Luo, S. Yang, W. Li, S. Lu, Y. Jin, L. Qiu and W. Zhang, *Small* 2020, **16**, 1906005.

25. Y. Zhang, Y. Hu, J. Zhao, E. Park, Y. Jin, Q. Liu and W. Zhang, *J. Mater. Chem. A* 2019, **7**, 16364-16371.

26. H. Li, J. Li, A. Thomas and Y. Liao, *Adv. Funct. Mater.* 2019, **29**, 1904785.

27. H. B. Aiyappa, J. Thote, D. B. Shinde, R. Banerjee and S. Kurungot, *Chem. Mater.* 2016, **28**, 4375-4379.

28. S. C. Shit, R. Singuru, S. Pollastri, B. Joseph, B. S. Rao, N. Lingaiah and J. Mondal, *Catal. Sci. Technol.* 2018, **8**, 2195-2210.

29. J. Li, Z. Cheng, M. Zhu, A. Thomas and Y. Liao, *ACS Appl. Energy Mater*. 2018, **1**, 6535-6540.

30. K. Dey, H. S. Kunjattu, A. M. Chahande and R. Banerjee, *Angew. Chem., Int. Ed.* 2020, **59**, 1161-1165.

31. M. Bhadra, S. Kandambeth, M. K. Sahoo, M. Addicoat, E. Balaraman and R. Banerjee, *J. Am. Chem. Soc.* 2019, **141**, 6152-6156.

32. Z. -A. Lan, G. Zhang, X. Chen, Y. Zhang, K. A. I. Zhang and X. Wang, *Angew. Chem. Int. Ed.* 2019, **58**, 10236-10240.

33. R. Tao, X. Ma, X. Wei, Y. Jin, L. Qiu and W. Zhang, *J. Mater. Chem. A* 2020, **8**, 17360-17391.

34. K. An and G. A. Somorjai, *ChemCatChem* 2012, **4**, 1512-1524.

35. M. L. Christian and K.-F. Aguey-Zinsou, *ACS Nano* 2012, **6**, 7739-7751.

36. L. Li, H. Zhao, J. Wang and R. Wang, *ACS Nano* 2014, **8**, 5352-5364.

37. W. Wang, C. Li, L. Yan, Y. Wang, M. Jiang and Y. Ding, *ACS Catal*. 2016, **6**, 6091-6100.

38. C. Li, W. Wang, L. Yan, Y. Wang, M. Jiang and Y. Ding, *J. Mater. Chem. A* 2016, **4**, 16017-16027.

39. W. Wang, Y. Wang, C. Li, L. Yan, M. Jiang and Y. Ding, *ACS Sustainable Chem. Eng*. 2017, **5**, 4523-4528.

40. S. A. Bhat, C. Das and T. K. Maji, *J. Mater. Chem. A* 2018, **6**, 19834-19842.

41. E. Oveisi, A. Letouzey, D. T. L. Alexander, Q. Jeangros, R. Schäublin, G. Lucas, P. Fua and C. Hébert, *Sci. Rep*. 2017, **7**, 10630.

42. H. Yue, Y. Zhao, S. Zhao, B. Wang, X. Ma and J. Gong, *Nat. Commun.* 2013, **4**, 2339.

43. R. Paul, S. C. Shit, H. Mondal, J. Rabeah, S. S. Kashyap, Y. Naliwal, D. B. Shinde, Z. Lai and J. Mondal, *ACS Appl. Nano Mater.* 2021, **4**, 11732-11742.

44. A. Vinu, K. Ariga, T. Mori, T. Nakanishi, S. Hishita, D. Golberg and Y. Bando, *Adv. Mater.* 2005, **17**, 1648-1652.

45. H. Wang, B. Hou, Y. Yang, Q. Chen, M. Zhu and A. Y. Thomas, *Small* 2018, **14**, 1803232.

46. J. V. Rojas, M. T. Gonzalez, M. C. M. Higgins and C. E. Castano, *Mater. Sci. Eng. B* 2016, **205**, 28-35.

47. Y. Li, Q. Wu, X. Guo, M. Zhang, B. Chen, G. Wei, X. Li, X. Li, S. Li and L. Ma, *Nat. Commun.* 2020, **11**, 599.

48. J. Sun, J. Yu, M. Ma, F. Meng, X. Wei, Y. Sun and N. Tsubaki, *Sci. Adv.* 2018, **4**, eaau3275.

49. C. Sarkar, R. Paul, S. C. Shit, Q. T. Trinh, P. koley, B. S. Rao, A. M. Beale, C. W. Pao, A. Banerjee and J. Mondal, *ACS Sustainable Chem. Eng*. 2021, **9**, 2136-2151.

50. G. D. M. R. Dabera, M. Walker, A. M. Sanchez, H. J. Pereira, R. Beanland and R. A. Hatton, *Nat. Commun.* 2017, **8**, 1894.

51. N. T. Bui, H. Kang, S. J. Teat, G. M. Su, C. W. Pao, Y. S. Liu, E. W. Zaia, J. Guo, J. L. Chen, K. R. Meihaus, C. Dun, T. M. Mattox, J. R. Long, P. Fiske, R. Kostecki and J. J. Urban, *Nat Commun.* 2020, **11**, 3947.

52. J. Mondal, A. Biswas, S. Chiba and Y. Zhao, *Scientific Reports* 2015, **5**, 8294.

53. J. Mondal, A. Modak, A. Dutta, S. Basu, S. N. Jha, D. Bhattacharyya and A. Bhaumik, *Chem. Commun.* 2012, **48**, 8000-8002.

54. T. Mitsudome, T. Urayama, K. Yamazaki, Y. Maehara, J. Yamasaki, K. Gohara, Z. Maeno, T. Mizugaki, K. Jitsukawa and K. Kaneda, *ACS Catal.* 2016, **6**, 666-670.

55. C. Wu, Y. Chen, R. Shen, W. Zhu, Y. Gong, L. Gu, Q. Peng, H. Guo and W. He, *Nano Research* 2018, **11**, 4883-4889.

56. A. Fedorov, H.-J. Liu, H.-K. Lo and C. Copéret, *J. Am. Chem. Soc.* 2016, **138**, 16502-16507.

57. N. Kaeffer, H.-J. Liu, H.-K. Lo, A. Fedorov and C. Copéret, *Chem. Sci.* 2018, **9**, 5366-5371.

58. S. Rej, M. Madasu, C.-S. Tan, C.-F. Hsia and M. H. Huang, *Chem. Sci.* 2018, **9**, 2517-2524.

59. S. Mao, B. Zhao, Z. Wang, Y. Gong, G. Lu, X. Ma, L. Yu and Y. Wang, *Green Chem.* 2019, **21**, 4143.

60. L. Shen, S. Mao, J. Li, M. Li, P. Chen, H. Li, Z. Chen and Y. Wang, *J. Catal.* 2017, **350**, 13-20.

61. N. Haque, S. Biswas, P. Basu, I. H. Biswas, R. Khatun, A. Khan and M. Islam, *New J. Chem.* 2020, **44**, 15446-15458.

62. R. Paul, S. C. Shit, T. Fovanna, D. Ferri, B. S. Rao, G. T. K. K. Gunasooriya, D. Q. Dao, Q. V. Le, I. Shown, M. P. Sherburne, Q. T. Trinh and J. Mondal, *ACS Appl. Mater. Interfaces* 2020, **12**, 50550-50565.

**Graphical Abstract:**

Product selectivity in catalytic semi hydrogenation of alkynes could be controlled by offering steric hindrance effect through organogel-assisted porous-organic-polymer (POP) supported Cu catalysts (Cu@TpRb-POP).